Nonlinear short-pulse propagation in a free-electron laser

Sang June Hahn and Jae Koo Lee
Department of Physics, Pohang Institute of Science and Technology, Pohang, Kyungbuk 790-600, Korea
(Received 31 March 1993)

With one-dimensional time-dependent Maxwell-Lorentz equations, we have numerically investigated the nonlinear short-pulse propagation in a free-electron laser (FEL). Considering the pulsed electron beam and the cavity detuning, we describe a spiking behavior and the dissipative dynamics in a FEL oscillator. We show that the spiking behavior is well understood by superradiant pulse propagation and its dynamical regimes are closely related to a bifurcation and the chaotic transition in the nonlinear dissipative dynamics. The scaled synchrotron slippage distance ($L_{\rm syn}/L_s$), where L_s is the slippage length and $L_{\rm syn}$ is the slippage distance in a synchrotron period, plays an important role in determining the dynamical regimes. Using dimensionless branching parameters, which are the cavity detuning parameter D, the slippage parameter S, and the superradiant parameter K, we describe the bifurcation and the chaotic transitions via a period-doubling cascade, an intermittency, and a quasiperiodicity. The real-time signal, the phase-space plot, and the corresponding power spectrum are used to confirm our results.

PACS number(s): 41.60.Cr, 52.75.Ms

I. INTRODUCTION

In this paper we numerically investigate nonlinear evolution of radiation pulses in a free-electron laser (FEL) which is driven by the periodically injected short-pulse electron beam. Using the nonlinear pulse propagation equations, we describe the spiking behavior in both single-pass amplifier and oscillator. We also describe the dissipative dynamics of the FEL oscillator by investigating the bifurcation and the chaotic transitions.

Since the first FEL was operated at Stanford [1], the FEL has become a very useful device in wide-ranged scientific applications, because of the potentiality of high-power and short-pulse radiation and tunable operations. In most FEL's operating in the infrared and visible spectral range, the electron beam is supplied by a rf accelerator and consists of a train of short micropulses. Because the short-pulse FEL has the possibility of achieving the picosecond time-scale radiation, which has many scientific applications, the subject of short-pulse propagation in the FEL has been experimentally and theoretically investigated.

For a long-pulse FEL, where the electron beam can be regarded as continuous, each section of electron beam evolves identically as it passes through the wiggler. Hence the relative slippage between electrons and radiation is neglected; this is known as the steady-state regime of the FEL [2]. If the electron pulses are sufficiently short, slippage makes each section of the electron pulse evolve not identically any more. Especially, in the high-gain regime, the short-pulse FEL propagation reveals several important and interesting issues of FEL physics. One is the spiking behavior in a free-electron laser, which is demonstrated in the experiments [3–5] and the simulations [6–10]. In a sufficiently saturated regime, the radiation pulse does not experience the usual steady-state saturation process, but breaks up into a series of narrow and high-intensity spikes. The spiking behavior is usually related to the low-frequency sidebands in the optical spectrum.

Recently, on the premise that the spiking behavior is basically related to the superradiant process, i.e., the amplification of spontaneous emission from noise, several investigators [8–10] have described the experimental optical spikes in terms of the superradiant pulse propagation in a single-pass FEL amplifier. Our previous work [10] shows that the evolution of radiation pulse in a high-gain FEL has two distinct dynamical regimes, defined by the two characteristic lengths; slippage length (L_s) and synchrotron slippage distance ($L_{\rm syn}$), which is the slippage distance in a synchrotron period ($T_{\rm syn}$), i.e., $L_{\rm syn} = \frac{(c-v_\parallel)}{v_\parallel} cT_{\rm syn}$ ($v_\parallel$ is the average axial velocity of the electron beam). For a superradiant regime, where $L_{\rm syn}$ is always greater than L_s, the spontaneous emission is generated in the trailing slippage region of the electron pulses. As the FEL interaction between electrons and radiation is enhanced, the synchrotron period shortens. When $L_{\rm syn}$ is equal to L_s, the pulse modulation starts and the narrow spikes are generated. For a spiking regime ($L_{\rm syn} < L_s$) the spikes continue to evolve to narrower and more intense ones. According to the recent work of Caloi [11], the spiking regime corresponds to the one where the superradiant instability [12–14] and the sideband instability [15] are seen to occur together. In this regime the low-frequency sidebands are clearly observed in its spectrum. In this paper, we will describe the spiking behavior in the FEL by the numerical simulation and the analogical interpretation of the superradiant pulse evolution in the high-gain single-pass FEL amplifier.

Another important issue is the nonlinear dissipative dynamics in the FEL oscillator. In a FEL oscillator, the radiation pulse bounces back and forth between cavity mirrors, gaining power while interacting with the electron pulse and losing power due to output coupling and losses.

Due to its open nature the FEL oscillator is treated as a nonlinear dissipative system as opposed to a Hamiltonian system of the FEL amplifier.

In a Hamiltonian FEL system, the effect of the self-electric and self-magnetic fields of the electron beam induces chaos in the single-particle trajectories in the vicinity of the gyroresonance in the presence of an axial magnetic field [16]. On the other hand, the dissipative FEL system, which concerns the self-consistent action and reaction of the electrons and the radiation, provides the various dynamical features. Since the study of bifurcation and chaos in a FEL is useful in understanding the characteristics of the radiation pulse and which operating regimes to avoid, it has become an important topic in the FEL physics [16–21]. The spiking regime in the nonlinear pulse propagation is closely related to the chaotic regime, where the irregular and strong sidebands are clearly observed; thus knowledge of the dissipative dynamics can also provide information about the spiking behavior.

In this paper, by considering the pulsed electron beam and the cavity detuning in the FEL oscillator, we will describe the bifurcations and the chaotic transitions; period doubling, intermittency, and quasiperiodicity [22,23].

This paper is organized as follows. In Sec. II we describe the nonlinear pulse propagation to describe the spiking behaviors. By considering the slippage and the cavity detuning, we also describe the optical spikes in a FEL oscillator. In Sec. III the bifurcation and chaotic transition in the dissipative oscillator system is considered in the parameter space of the relevant physical parameters. The paper concludes with a general discussion in Sec. IV.

II. THE SPIKING BEHAVIOR IN A FREE-ELECTRON LASER

A. The amplifier configuration

In this section, we will describe the spiking behavior in the FEL amplifier using the nonlinear pulse propagation equations. Because of the finite slippage between electrons and radiation pulses, the spatio-temporal interaction of the FEL is classified into three different processes. They are the steady-state process in the body of electron pulse, the radiation-decay process in the leading edge, and the superradiant process in the trailing edge. In the superradiant region (i.e., the trailing slippage region), the field is space-time dependent and the electrons do not evolve identically any more; this is basically related to the reduced radiation reabsorption due to the continuous radiation escape, which would inhibit any steady-state saturation process and make the superradiant scaling. According to the previous works on the superradiance [6,8,12,13], by introducing a dimensionless parameter K, two different regimes are defined [$K = L_c/L_e$, where L_e is the electron pulse length, $L_c = \lambda/4\pi\rho$ is the cooperation length, and $\rho = 1/\gamma(a_w\omega_p/4ck_w)^{2/3}$ is the fundamental FEL parameter; ω_p is the plasma frequency]. In the short-pulse regime ($K > 1$; $L_e < L_c$), the superradiant process is dominant (no steady-state process exists), with peak intensity proportional to n_e^2 (where n_e is the electron beam density). In the long-pulse regime ($K \ll 1$; $L_e \gg L_c$), the steady-state process is dominant except for the trailing region. However, in the high-gain regime, the radiation in the trailing slippage region exhibits the superradiant spiking behavior with radiation intensities much greater than the steady-state saturated values.

To understand the superradiant process more qualitatively, we review the radiation damping model [12], which considers the slippage effect simply by introducing an exponential loss term of the radiation field, proportional to $e^{-\alpha z}$, in the steady-state equations [24]. In this damping model, the damping constant (α) for the field amplitude corresponds to the spatial decay rate, i.e., the reciprocal of the interaction length ($L_{\rm int}$) in the laboratory frame ($\alpha = L_{\rm int}^{-1} = L_e\beta_\parallel/1-\beta_\parallel$, and $\beta_\parallel = v_\parallel/c$), which becomes the superradiant parameter K in the scaled coordinate $\bar{z} = (4\pi\rho/\lambda_w)z$ [13]. Figure 1 shows the instability domains obtained from the linear dispersion relation of the damping model. As shown in Fig. 1, when the energy detuning δ [$= (1/2\rho)(\gamma_0^2-\gamma_r^2)/\gamma_r^2$, where γ_r is the resonance energy and γ_0 is the initial injection energy] is greater than the steady-state threshold $\delta_T = (3/2)^{2/3} \simeq 1.89$ [2], the superradiant solution solely exists and becomes rather larger as K increases. This reflects the intrinsic property of superradiance, i.e., the superradiant pulse evolution is just due to the amplification of spontaneous emission (ASE) [25], which is resonant with the initial injection energy, γ_0.

To describe the self-consistent nonlinear interaction of the radiation pulse with the electron pulse, we use the usual one-dimensional coupled Maxwell-Lorentz equations [10,13] for the electron phase $\theta = (k_s + k_w)z - \omega_s t$ and the complex radiation field $\tilde{a} = a_s \exp(i\phi_s)$.

$$\frac{\partial}{\partial x}\gamma_j = -\frac{k_s a_s a_w}{\gamma_j}\sin(\theta_j + \phi_s), \tag{2.1}$$

$$\frac{\partial}{\partial x}\theta_j = k_w - k_s\frac{(1+a_w^2)}{2\gamma_j^2}, \tag{2.2}$$

$$\frac{\partial}{\partial y}\tilde{a} = i\eta F(y)a_w\left\langle\frac{e^{-i\theta}}{\gamma}\right\rangle, \tag{2.3}$$

where $j = 1,\ldots,N$; a_s, k_s and a_w, k_w are the normalized field amplitudes and the wave numbers of the radi-

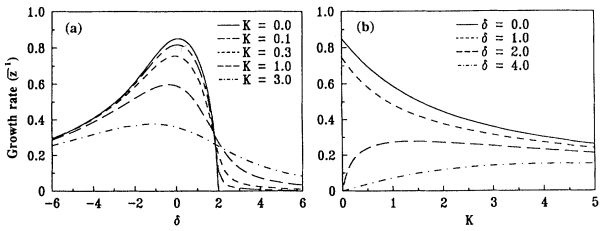

FIG. 1. Linear dispersion theory. (a) Growth rate vs energy detuning (δ) for several values of K. (b) Growth rate vs K for several values of δ. $\rho = 0.01$.

TABLE I. Fundamental parameters used in the simulations.

Facility	γ	a_w	λ_w (cm)	λ (μm)	L_s (λ)	L_e (λ)	L_c (λ)[a]	R (%)[b]
PALADIN (Ref. [7])	111	1.21	10	10.0	200	300	8.3	
FELIX (Ref. [27])	49.02	1.20	6.5	33.0	38	30	21.1	5.0
LANL (Ref. [3])	45	0.7874	2.5	10.0	40	800	26.4	7.0

[a]They correspond to 2000, 70, and 70 Å, respectively.
[b]Total cavity loss.

ation field and the undulator, respectively. In Eq. (2.3), $x = v_\parallel(ct-z)/(c-v_\parallel)$ and $y = c(z-v_\parallel t)/(c-v_\parallel)$, which are proportional to the retarded times at the speed of the electrons $v_\parallel$ and the speed of light c, respectively; $\eta = \omega_p^2/2k_s c^2$ is the coupling strength, $F(y)$ is the macroscopic axial electron beam profile function [$0 < F(y) \leq 1$ inside the electron pulse] and the symbol $\langle\,\rangle$ denotes an ensemble average over electrons.

In this simulation study, the nominal PALADIN parameters [7] are used (see Table I). For the typical run, we use the top-hat profile of the electron pulse, i.e., $F(y)=1$ inside the pulse and assume that the initial excitation is distributed over the entire electron pulse. The calculations from the nonlinear pulse propagation equations (2.1)–(2.3) are compared with those of the damping model. As shown in Fig. 2, the results from the damping model are very consistent with those of nonlinear pulse propagation equations except for the high current regime (which corresponds to the strong superradiant regime in Refs. [6,13], where $K \ll 1$). As the electron pulse length decreases (i.e., K increases), the scaling of the peak power ($\check{P}$) and the efficiency (η) tends to reach the superradiant scaling; $\check{P} \propto I^2$ and $\eta \propto \sqrt{I}$ [9]. Because of the continuous energy extraction from the electron pulse, the superradiant process results in the dramatic increase of the efficiency η for the short-pulse regime ($K > 1$). However, the considerable portion of the extracted energy is contained in the escaping leading part of the radiation, so that the effective efficiency ($\eta_{\rm eff}$), which is the net efficiency excluding the contribution of the lost power (i.e., $\eta_{\rm eff} = \eta - \eta_{\rm loss}$), is always less than that of steady-state theory [see Fig. 2(b)]. According to this study, it is shown that the superradiant scaling comes from the relatively low coupling in the low current regime (i.e., small ρ and large K), not from the enhanced mechanism as in the laser physics.

To describe the superradiant pulse evolution only, we consider the positive detuning regime ($\delta > \delta_T$) where the steady-state solution does not exist. As shown in Fig. 3, the evolution of the superradiant pulse is characterized by the scaled synchrotron slippage distance ($L_{\rm syn}/L_s$) and the spike velocity (in this paper, it means the velocity of the main peak of the pulse). In the superradiant regime

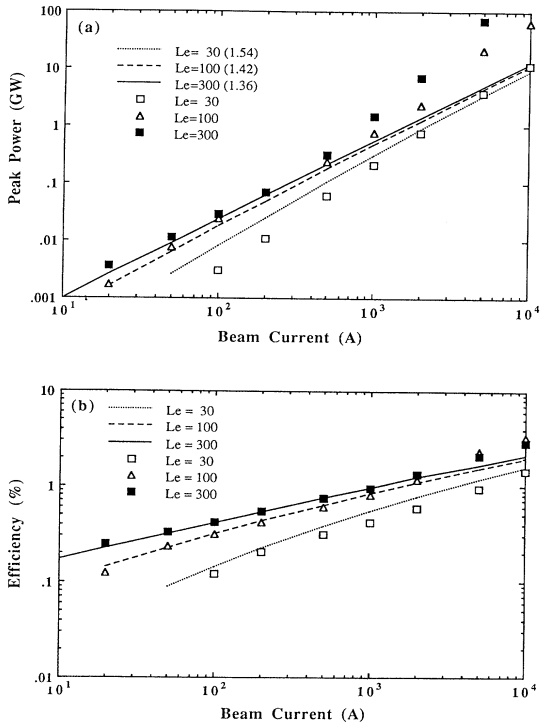

FIG. 2. Peak power intensity ($\check{P}$) (a) and extraction efficiency (b) vs beam current (I) for $L_e = 30\lambda$, 100λ, and 300λ. All lines represent the results calculated from the damping model. The numerical values in the parentheses are the slopes of the linear fitting (steady-state regime: $\check{P} \propto I^{4/3}$, superradiant regime: $\check{P} \propto I^2$). The symboled points are our simulation results using Eqs. (2.1)–(2.3).

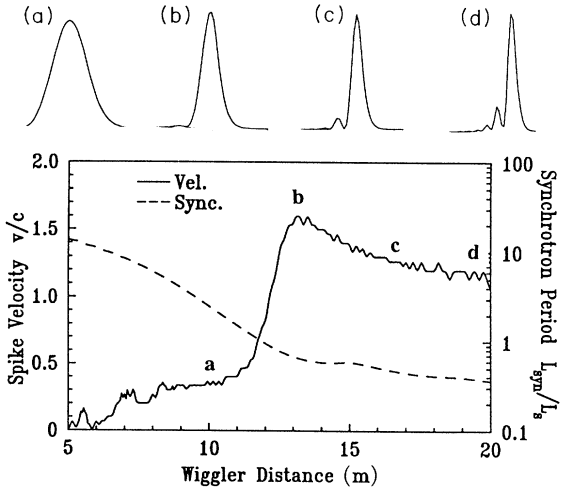

FIG. 3. Spike velocity and scaled synchrotron slippage length as a function of wiggler distance. The four figures on the top are the radiation pulse profiles at the specific positions (a: 10 m, b: 13 m, c: 17 m, and d: 20 m).

($L_{\rm syn} > L_s$; around point a in Fig. 3), the initial spontaneous emission keeps growing with the shape unchanged (slightly distorted Gaussian-like shape due to the laser lethargy) and the frequency modulation is clearly observed. The spike velocity is always less than the speed of light because the peak position of the pulse falls back, and the pulse width [full width at half maximum (FWHM)] is approximately half of the slippage length ($\sim \frac{1}{2}L_s$). When $L_{\rm syn}$ is equal to L_s (near the point b in Fig. 3), the pulse modulation by the synchrotron oscillation starts. As the synchrotron period decreases the trailing edge of the pulse erodes by the absorption process, so that the spike velocity becomes greater than c. The pulse width becomes approximately half of the synchrotron slippage distance ($\sim \frac{1}{2}L_{\rm syn}$). This is the spiking regime (around point c in Fig. 3) where the long-wavelength sidebands are clearly observed. As the spike intensity continues to grow, the strong pulse modulation continues and the main spike with the trailing small-intensity spikes becomes narrower. In this high-spiking regime (near point d in Fig. 3) the spike velocity comes down to the light velocity due to the diminishing lethargy effect and the spectrum becomes broad and chaotic.

B. The oscillator configuration

In this section, we investigate the optical spikes [3–5] in the FEL oscillator through the superradiant spiking model and the multipass simulation using Eqs. (2.1)–(2.3). Considering the effects of the slippage and the cavity detuning, we describe the various features of the nonlinear pulse propagation in the FEL oscillator for both short-pulse ($L_e \sim L_s$) and long-pulse ($L_e \gg L_s$) cases.

1. The short-pulse case: $S \sim 1$ ($L_e \sim L_s$)

In the FEL oscillator driven by the pulsed electron beams, the emerging radiation has a temporal structure which also consists of pulses. In such a system the radiation and the electron pulse overlap within the interaction region. Hence it is necessary to synchronize the radiation with the successive beam micropulses, thus providing for spatio-temporal overlap between radiation and electron pulses. If the electron pulse length is comparable with the slippage ($L_e \sim L_s$), because of the well-known laser lethargy effect [26] the radiation slows down compared to the vacuum speed of light c. To compensate for this lethargy, it is necessary to slightly advance the radiation pulse by reducing the cavity length by a distance δL.

For the simulation of the short-pulse case ($L_e \sim L_s$), we use free-electron laser for infrared experiments (FELIX) parameters [27]; the electron pulse length (L_e) is approximately 30λ and the slippage length (L_s) is 38λ (all parameters used are listed in Table I). To compare with the experimental results we use the realistic current distributions, $F(y)$ (Gaussian, Lorentzian-like, and top hat). Figure 4 shows the radiation pulse profiles at the entrance of the wiggler. As shown in Fig. 4, the temporal evolution of the radiation pulse is very similar to that of the amplifier configuration (see Fig. 3). This

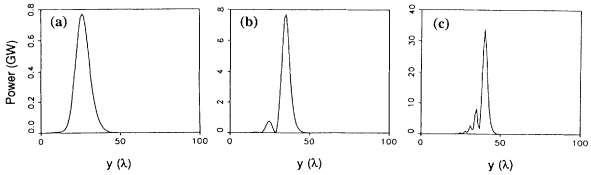

FIG. 4. Short-pulse case ($L_e \sim L_s$). Radiation pulse profiles at pass 50 (a), 100 (b), and 200 (c).

similarity reflects the fact that the spiking behavior in the FEL oscillator can be described by the superradiant spiking model in the single-pass amplifier. As Bonifacio, Piovella, and McNeil [8] first proposed, the multipass interaction in the oscillator can be considered qualitatively equivalent to a single-pass FEL with a long wiggler in which an initial short radiation pulse (L_r) propagates over a long electron pulse ($L_e > L_r$), starting from its trailing edge. The situation of the periodically injected fresh (i.e., unperturbed) electron micropulse in the oscillator is simply replaced by that of the long unperturbed electron pulse in the amplifier. The electron pulse length is chosen to be greater than the sum of the radiation pulse length and the slippage length ($L_e > L_r + L_s$) such that the electron pulse is regarded as effectively infinite. The equivalent situation is also made such that the initial radiation pulse excited over the entire electron pulse ($L_r = L_e$) propagates through the electron pulse with the detuned energy ($\delta > \delta_T$), which is just the case of Fig. 3.

Up to now, we have treated the case of the perfect synchronism ($\delta L = 0$). If we consider the cavity detuning, the full system undergoes the dramatic change in its characteristics, which may be the inherent property of the short-pulse FEL oscillator. Figure 5 shows the radiation pulse profiles and their power spectra at pass 400 for the different cavity detunings; $\delta L = -0.5\lambda$, -1.0λ, and -2.0λ. According to the previous study on the cavity detuning in the FEL oscillator [21] the cases of $\delta L = -1.0$ and -2.0λ correspond to the periodic oscillation regime (in view of the nonlinear dynamics, it relates the limit cycle [22] in the phase space, thus it is also called limit-cycle oscillation) and the case of $\delta L = -0.5\lambda$ corresponds to the chaotic regime. The pulse profiles in Fig. 5 consist of several narrow pulses which are modulated by $L_{\rm syn}$, not by L_s. The pulse separations in the radiation pulse profiles nearly correspond to the synchrotron slippage distance ($L_{\rm syn}$) and the fundamental frequency in the power spectrum, which has its regular harmonics in Figs. 5(b) and 5(c), is proportional to $L_{\rm syn}/|\delta L|$.

As shown in Fig. 6 the limit-cycle oscillation (LCO) is clearly observed and the period decreases as the detuning increases. Recently, Jaroszynski *et al.* [28] first observed the limit-cycle oscillation of the radiation power in the FELIX experiment. By considering the slippage and the cavity detuning, they proposed a simple formula of the LCO period as follows:

$$\tau = \frac{L_s}{2|\delta L|}\tau_c, \tag{2.4}$$

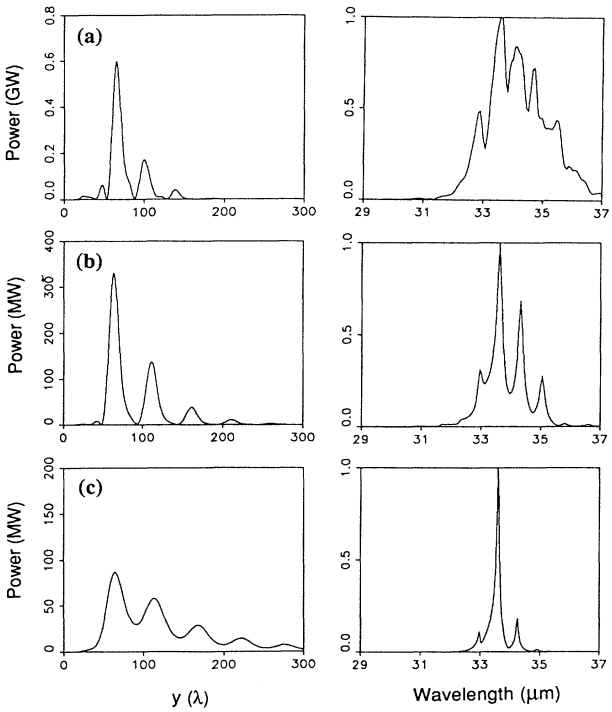

FIG. 5. Radiation pulse profiles and spectral power distributions for $\delta L = -0.5\lambda$ (a), -1.0λ (b), and -2.0λ (c).

where τ_c is the time for a radiation pulse to bounce back and forth inside the cavity. However, as mentioned before, the role of L_s should be replaced by that of $L_{\rm syn}$ because the dynamics in the FEL is governed by $L_{\rm syn}$, not by L_s, so that

$$\tau = \frac{L_{\rm syn}}{2|\delta L|}\tau_c \ . \tag{2.5}$$

As shown in Fig. 7, the revised formula is very consistent with the experimental data [21,28].

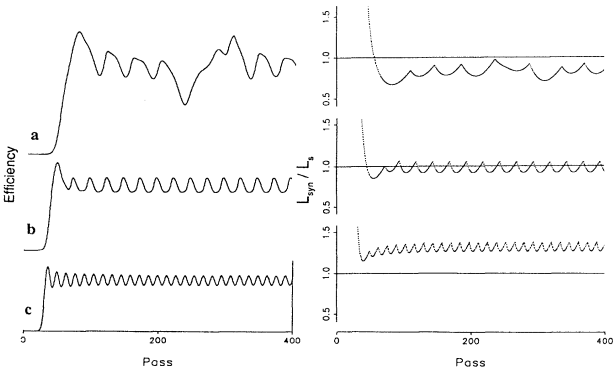

FIG. 6. Time history of the extraction efficiency and the scaled synchrotron slippage length ($L_{\rm syn}/L_s$) for $\delta L = -0.5\lambda$ (a), -1.0λ (b), and -2.0λ (c).

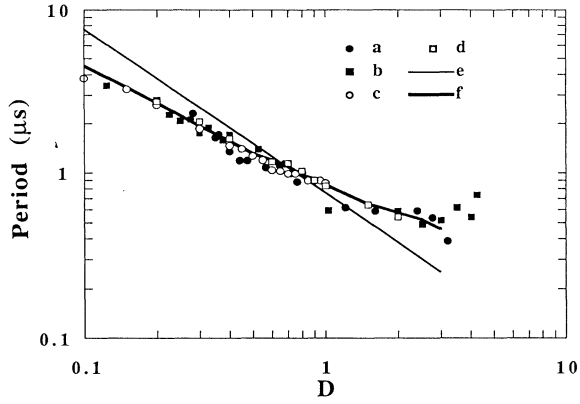

FIG. 7. Period of the limit-cycle oscillation as a function of D for $S = 1.267$, $K = 0.787$. Experiments (Ref. [28]) (a: $\lambda = 25$ μm, b: 40 μm) and numerical calculations (c: 33 μm in Ref. [28], d: 33 μm in Ref. [21]). The solid lines e and f represent the theoretical results of Refs. [28] and [21], respectively.

2. *The long-pulse case: $S \ll 1$ ($L_e \gg L_s$)*

In the long-pulse case such as the ones operating at Los Alamos [3] the periodic spikes were observed at high saturated power, and the spiking period stayed approximately fixed, equal to the slippage length (L_s). The superradiant pulse propagation may also explain the periodic spiking behavior by considering such a long pulse as consecutive subdivision, each of length equal to the slippage length, and each developing a single optical spike [8–10]. In this simulation we use the parameters of the Los Alamos National Laboratory (LANL) FEL [3] (see Table I); the electron pulse length is taken to be approximately 20 times the slippage distance ($L_e = 800\lambda$ and $L_s = 40\lambda$). Throughout the simulation study the periodic multispike is observed as shown in Fig. 8 and the usual sidebands are clearly observed in its spectrum. Since only the leading part of the radiation sees completely freshly injected electrons, the initial spikes are generated first at the leading edge of the radiation pulse. As the interaction is enhanced, at the highly saturated power the radiation pulse becomes modulated by the envelope of the electron pulse (in this study we use the Gaussian electron pulse).

The multispiking behavior in the long-pulse case may also be understood by the superradiant pulse propagation in a single-pass FEL. As shown in Fig. 9, we consider the amplifier simulation such that the initial radiation pulse length L_r is much larger than L_c ($L_r = 100\lambda$ and $L_c = 8.3\lambda$) for the resonant and the detuned cases. Clearly, in the resonant case, the usual trailing edge spike is overwhelmed by the strong leading edge spike. This reflects the fact that better amplification of the superradiant pulse occurs when it interacts with the unperturbed electrons. On the other hand, for the detuned case ($\delta > \delta_T$, $\delta = 6.10$), twin spikes are observed at the initial spiking stage and at a later stage the trailing spike intensity becomes less than that of the leading edge spike. This is because the electron pulse is perturbed by the leading

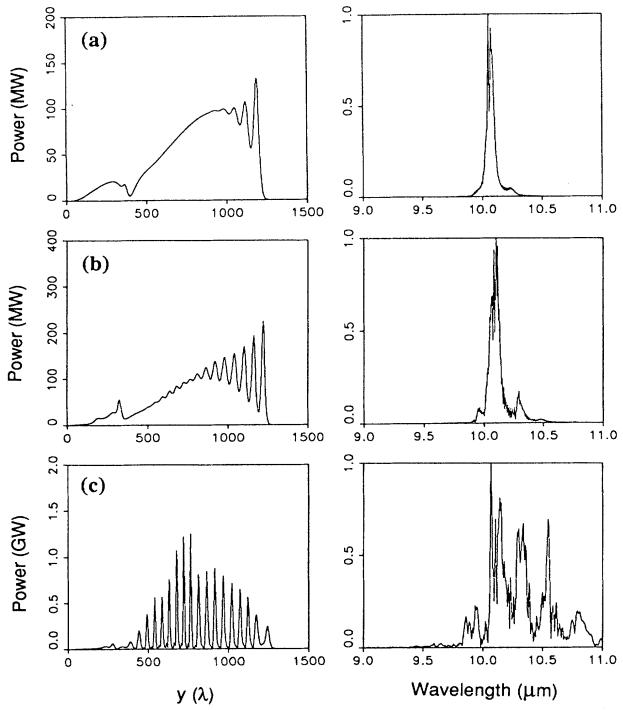

FIG. 8. Long-pulse case ($L_e \gg L_s$). Radiation pulse profiles and spectral power distributions at pass 150 (a), 250 (b), and 400 (c).

edge spike. The first notable result in this simulation is that the separation between two spikes is approximately fixed, equal to L_r, which may be relevant to the multispiking behavior with the fixed separation of L_s. The second notable result is that when L_c becomes greater than or comparable to L_r (i.e., low-coupling regime, low ρ), the leading and the trailing spike cannot resolve each other. This situation is quite analogous to the spiking behavior of the FEL oscillator when L_c is greater than L_s. The Stanford FEL [4], though L_e is much greater than L_s, does not show the usual well-defined high-intensity multispiking behavior, which is due to the relatively large L_c compared with L_s (for the Stanford FEL, $L_e \simeq 250\lambda$, $L_s = 47\lambda$, $L_c \simeq 1320\lambda$, and $\rho = 6.0 \times 10^{-5}$).

The measured FWHM of the spike in Fig. 8 is approximately 10λ, which corresponds to 0.3 ps. Our result is very close to the experimental [3] and the analytical values [29], which are 0.25 and 0.24 ps, respectively.

In the long-pulse case, the laser lethargy effect is very small compared with the short-pulse case, thus the power level rather decreases in presence of the detuning (not shown here). Figure 10 shows the radiation pulse profiles for $\delta L = -0.5\lambda$, -1.0λ, and -2.0λ. In addition to the leading edge spike, there exists another spiking region, which corresponds to the strong-coupling region in the electron pulse (i.e., high density region). The pulse separation between spikes is nearly fixed to L_s irrespective of the cavity detuning.

As shown in Fig. 11 the radiation power intensity and its characteristics are insensitive to the energy detuning for both cases of short- and long-pulse FEL oscillators, which reveals the property of the superradiant pulse evolution (the short-pulse case is not shown here but the similar results are observed). According to the previous study on the superradiant spiking [8,10,13], the peak power intensity of the detuning case ($\delta > \delta_T$) is rather greater than that of the resonant case. However, in the oscillator simulations, the reverse situation is observed. This is simply because of the relatively short slippage length (L_s) compared to the cooperation length L_c, which can be interpreted as a measure of the minimum distance between which electrons may interact cooperatively via the radiation field [the amplifier case: $L_s = 200\lambda$, $L_c = 8.3\lambda$; the oscillator case: $L_s = 38\lambda$, $L_c = 21.1\lambda$ (FELIX) and $L_s = 40\lambda$, $L_c = 26.4\lambda$ (LANL)].

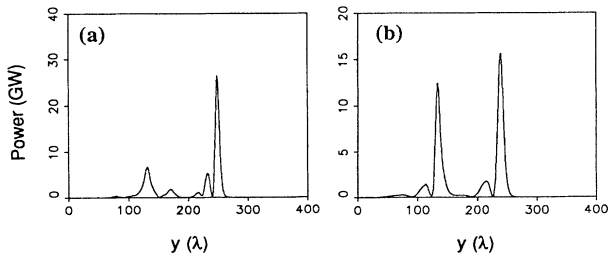

FIG. 9. Amplifier simulation. Radiation pulse profiles at the exit of the wiggler ($z = 20$ m): (a) resonant case ($\gamma_0 = 111$) and (b) detuned case (γ_0=117, δ=6.10). $L_e = 300\lambda$, $L_r = 100\lambda$ and top-hat profile.

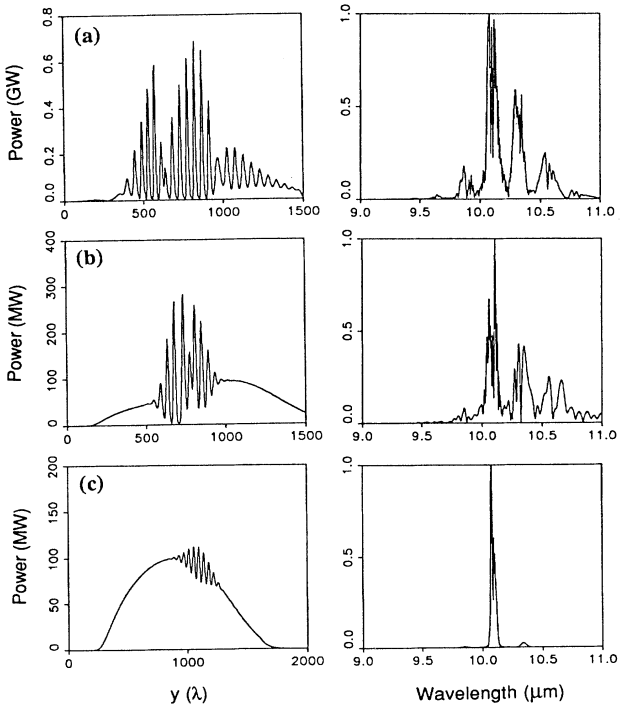

FIG. 10. Radiation pulse profiles and spectral power distributions at pass 400 for $\delta L = -0.5\lambda$ (a), -1.0λ (b), and -2.0λ (c).

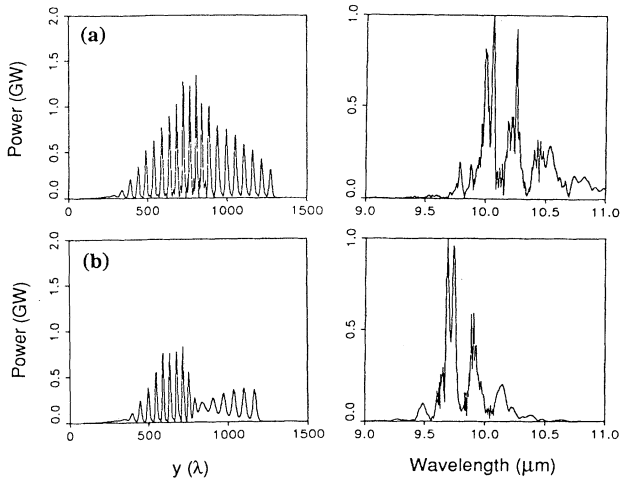

FIG. 11. Radiation pulse profiles and spectral power distributions at pass 400 for $\delta = 2.26$ (a) and 7.40 (b).

III. THE DISSIPATIVE DYNAMICS IN A FEL OSCILLATOR

In this section, we describe the nonlinear dissipative dynamics of the FEL oscillator. As mentioned in the preceding section, due to the inherent open nature of the oscillator, the self-consistent action and reaction of the electrons and the radiation provides the nonlinear dynamical problems [17–21]. According to the previous studies on the FEL oscillator [17,18,20], it is shown that as the beam current increases (three or four times the threshold current) the single-frequency equilibrium solution becomes unstable and then quasiperiodic and chaotic. Using the self-consistent set of equations, Bogomolov *et al.* [17] investigated the stationary and the pulsed injection regime. They showed that as the beam current increases there exists the bifurcative transition from the stationary single-mode generation to the stochastic self-modulation and that the self-modulation of the radiation pulse is due to the overbunching instability (i.e., sideband instability). In the recent work of Antonsen [20], he showed that there exists the chaotic route via the period-doubling cascade in the FEL oscillator system, which is driven by the continuous beam. By using a one-dimensional simple return map equation he has demonstrated the chaotic transition through the bifurcation diagram and the Lyapunov exponent [22]. He also showed that as the beam current increases, the radiation field changes from single frequency to broadband and chaotic. However, since all previous works were restricted to the simple case of the continuous beam or the perfect synchronism, the bifurcation and the specific chaotic routes in the full system, where the pulsed electron beam and the cavity detuning are concerned, could not be described. Very recently, Hahn and Lee [21], considering the pulsed electron beam and the cavity detuning, described the bifurcation and the chaotic transition using the self-consistent nonlinear pulse propagation equations (2.1)–(2.3). The chaotic transition via period-doubling cascade was found and the characteristics in the different dynamical regimes were shown to be correlated with the superradiant spiking model.

A. Bifurcative transition to chaos

In this paper, to see the spatio-temporal evolution of the radiation pulse and to investigate the bifurcations, the following branching parameters are used: D $(= \delta L/\lambda)$, S $(= L_s/L_e)$, and K $(= L_c/L_e)$. These parameters are closely related to the real physical parameters such as the electron beam current (I), the electron pulse length (L_e), and the wiggler length (L_w). Figure 12 shows a phase diagram for $D = -0.5$, -1.0, and -2.0. As shown in Fig. 12, the chaotic region is made in the high current, long wiggler, long-pulse, and small cavity detuning regimes, which correspond to the higher nonlinear coupling regime, and the stable focus region (i.e., stationary single-mode region) is made in the opposite situation. The bifurcative transition from the stable focus to chaos is made via well-known Hopf bifurcation and period-doubling cascade [22,23].

For the description of the dissipative dynamics in the FEL oscillator, we define the fundamental branching parameter μ as the reciprocal of the scaled synchrotron slippage distance $(\mu \equiv L_s/L_{\rm syn})$, which has a role similar to that of the Rayleigh number in the Rayleigh-Bérnard convection system [22]. The parameter μ is a complicated function of S, K, and D and represents the strength of nonlinear coupling between electrons and radiation. In the stable focus region $(\mu < 0.8)$ the radiation pulse becomes quasicontinuous (i.e., no subpulses develop) because of the low gain and the large damping. Its power spectrum has a single peak which corresponds to the inverse of the LCO period of Eq. (2.4). This stationary single-mode region is closely related to the superradiant

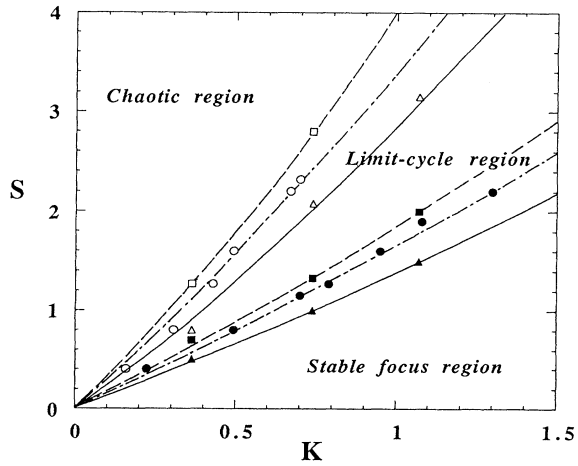

FIG. 12. Phase diagram. Symboled points are determined by the simulation. The curves are made by simple data fittings. Filled symbols represent Hopf bifurcation points and open symbols represent period-doubling bifurcation points. Rectangle, $D = -0.5$; circle, $D = -1.0$; and triangle, $D = -2.0$.

regime in the superradiant spiking model. In the limit-cycle region ($0.8 < \mu < 1.5$), the single-mode equilibrium becomes unstable, the radiation amplitude varies periodically. The distinct subpulses develop and the spectrum shows narrow sidebands separated by $\lambda/\mu N_w$, where N_w is the total number of the wiggler period (see Fig. 5). In this study, the values of μ at the lower and upper bounds of the bifurcative dynamical region are roughly estimated through the self-consistent simulations.

In the period-doubling region ($1.5 < \mu < 2.0$), as the sequential period doubling occurs, the sidebands in the spectrum are also sequentially doubled. In the chaotic region ($\mu > 2.0$), the radiation pulse becomes irregular in its shape and the power spectrum becomes broad and chaotic. This region corresponds to the spiking regime, where the usual sideband instability is dominant.

B. Quasiperiodicity and intermittency

In this study, in addition to the period-doubling chaotic transition, we have found new chaotic transition routes via quasiperiodicity and intermittency [22,23]. In the range of $\mu = 1.2$–1.8, the quasiperiodicity and the intermittency are clearly observed. Quasiperiodicity is associated with the Hopf bifurcation [22], which introduces a new frequency into the system. According to the theoretical work of Ruelle, Takens, and Newhouse (cited in [23]), after two or three sequences of Hopf bifurcation, the regular motion becomes highly unstable in favor of motion on a strange attractor. Figure 13 shows the time history of the extraction efficiency, phase-space plot, and the power spectrum for three different μ's. Three figures represent the chaotic, three-frequency quasiperiodic and two-frequency quasiperiodic phases, respectively. As shown in Fig. 13, there exists the chaotic phase in the smaller μ regime, which reveals the fact that there exist many other routes to chaos in a complicatedly combined way of the three main routes to chaos; period doubling, quasiperiodicity, and intermittency.

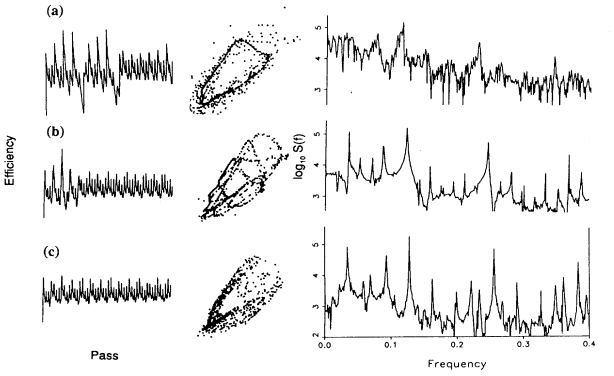

FIG. 13. Quasiperiodic route to chaos. The extraction efficiency, phase-space plot, and power spectrum $S(f)$ for three different beam currents; I = 400, 460, and 500 A, which correspond to $\mu = 1.41$, 1.45, and 1.50, respectively. The frequency f in the figure corresponds to T ($T = f^{-1}\tau_c$) in the time domain. $D = -2.0$ and $S = 1.0$.

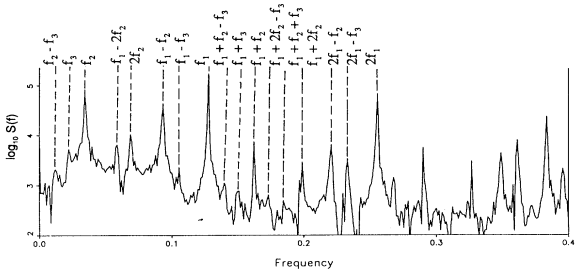

FIG. 14. Power spectrum $S(f)$ for I = 500 A [in the case of (c)]. f_1, f_2, and f_3 are the fundamental frequencies and the specified peak positions are determined by the least-squares fittings.

To confirm the existence of the three-frequency quasiperiodicity, we analyze the power spectrum of Fig. 13(b). As shown in Fig. 14 the three-frequency quasiperiodic spectrum can be represented as the linear combinations of the three fundamental frequencies; f_1, f_2, and f_3. In this case, the ratios between the fundamental frequencies are all incommensurate as expected ($f_2/f_1 \simeq 0.269$, $f_3/f_1 \simeq 0.174$, and $f_3/f_2 \simeq 0.645$).

Intermittency means the occurrence of a signal that alternates randomly between long regular phases and relatively short irregular bursts. This chaotic route via intermittency is associated with a "saddle-node bifurcation" (inverse tangent bifurcation), i.e., the collision of a stable and unstable fixed point which then both disappear [22,23]. Figure 15 shows the first simulational observation in a FEL of the typical transition from the regular LCO phase to the chaotic phase via "type-I" intermittency [22,23]. As shown in Fig. 15(b), there exists the two-frequency quasiperiodic phase as an intermediate phase. Though not shown here, after the chaotic phase, the regular LCO or two-frequency quasiperiodic phase is returned. Since the type-I intermittency is closely related to the $1/f$ noise [22], whose power spectra diverge at low

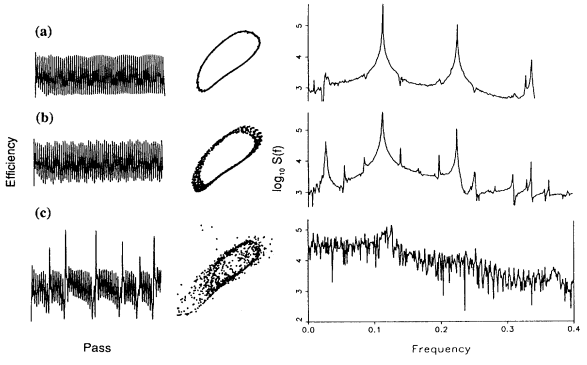

FIG. 15. Intermittent route to chaos. The extraction efficiency, phase-space plot, and power spectrum $S(f)$ for three different beam currents; I = 660, 665, and 695 A, which correspond to $\mu = 1.15$, 1.16, and 1.26, respectively. $D = -2.0$ and $S = 0.8$.

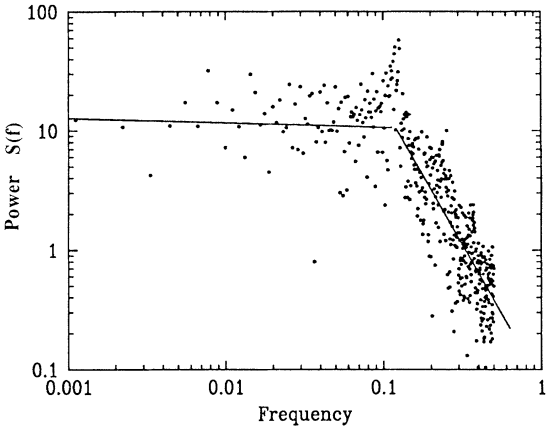

FIG. 16. Low-frequency spectral noise power dependence on frequency. The data are the same as presented in Fig. 15(c) for $I = 695$ A but are replotted on a log-log plot.

frequencies with a power law $1/f^{\delta}$ $(0.8 < \delta < 1.4)$, we analyze the low-frequency noise as displayed on a log-log plot in Fig. 16. At the onset of chaos, a power-law spectrum is observed with a scaling relationship of $f^{-2.3\pm0.4}$. This scaling agrees with results from numerical simulations [30] and the experiment [31] of type-I intermittency, where their spectra with f^{-2} scaling were observed. Below $f \sim 0.1$, the noise power is almost constant with frequency, which is due to perturbation by inherent white noise. With the discovery of the quasiperiodic and intermittent chaotic routes, our study notes that the bifurcation and the chaotic transition in the FEL dynamics has the complicated structure.

IV. DISCUSSION

In this paper we have investigated the spiking behavior and the dissipative dynamics in the free-electron lasers. Throughout this study, it is shown that the scaled synchrotron slippage distance ($L_{\rm syn}/L_s$) plays a crucial role in determining the dynamical regimes. In the superradiant spiking model, when $L_{\rm syn} > L_s$, the superradiant instability is dominant and when $L_{\rm syn} < L_s$ the usual sideband instability is dominant.

In the dissipative dynamics of the FEL oscillator, the principle branching parameter μ is the reciprocal of the scaled synchrotron slippage distance ($\mu = L_s/L_{\rm syn}$). The transition point ($L_s = L_{\rm syn}$, $\mu = 1$) between the superradiant regime and the spiking regime nearly corresponds to the Hopf bifurcation point [21]. When $\mu > 1$, the sideband instability becomes dominant which makes the power spectrum broad and chaotic through a sequence of period doublings and/or a sequence of frequency splittings involving quasiperiodic frequencies.

In the amplifier configuration, the superradiant spiking shows the dramatic increase of the peak radiation power which is much greater than the steady-state saturated values. This is due to the relatively long interaction length (i.e., $L_s \gg L_c$) and the strong coupling in the trailing slippage region in the case of the top-hat profile. According to the previous study [10], the intensity of the superradiant spiking is considerably reduced in the case of realistic beam profiles, which does not obey the superradiant scaling any more. In the oscillator configuration, since the usual operation regime corresponds to the short-interaction-length regime (i.e., $L_s \sim L_c$), the superradiant spiking such as in the FEL amplifier does not grow and thus the profile effect of the electron pulse is negligible. According to the work of Graham and Isermann [32], the superradiant spiking may be caused by the spatial inhomogeneity introduced at the trailing edge of the electron pulse. By taking into account the shot noise, they showed that instead of the high-intensity spikes, there exist rather smaller intensity pulses appearing from shot noise throughout the electron pulse. Similar results were also observed in our previous work [10], but the effect of shot noise was negligible. In addition to the shot-noise effect, the effects of energy spread and space-charge field are expected to be important in the nonlinear spiking behavior. As a further study, based on our formulation of the space-charge field [33], we will investigate the space-charge effect on the spiking behavior.

In this paper, using the self-consistent pulse propagation equations, we describe the bifurcation and chaotic transition in terms of the relevant branching parameters; S, K, and D. In the parameter space of S, K, and D we specify the dynamical regimes which show the different characteristics in the nonlinear pulse propagation. To show the difference of the dynamics at the different spatial locations, we measure the radiation amplitude and phase at several specific positions of the electron pulse in the electron rest frame. Since only the leading part is affected by the fresh electron pulse, it is expected that the leading part of the radiation pulse evolves faster than the trailing part. However, the difference of dynamics turns out to be negligible in the short-pulse FEL.

Throughout this study we found that there may exist many other substructures in the well-defined phase diagram in Fig. 12. These substructures may consist of the periodicity, the two-frequency quasiperiodicity, the three-frequency quasiperiodicity, the intermittency, and the chaos. Though the full system is controlled by the fundamental parameter μ, because of the inherent complexity of μ, the overall dynamical features must be described in terms of S, K, and D. The work on this topic is progressing with the detailed discussion and results planned to appear in a forthcoming paper.

ACKNOWLEDGMENTS

Helpful discussions with Professor Seunghwan Kim are gratefully acknowledged. This work was supported in part by Korean Science and Engineering Foundation (Center for Thermal and Statistical Physics) and Ministry of Education (Basic Science Research Institute).

[1] D. A. G. Deacon, L. R. Elias, J. M. J. Madey, G. T. Ramian, H. A. Schwettman, and T. I. Smith, Phys. Rev. Lett. **38**, 892 (1977).
[2] R. Bonifacio, C. Pellegrini, and L. Narducci, Opt. Commun. **50**, 373 (1984).
[3] R. W. Warren, J. C. Goldstein, and B. E. Newnam, Nucl. Instrum. Methods A **250**, 19 (1986).
[4] B. A. Richman, J. M. J. Madey, and E. Szarmes, Phys. Rev. Lett. **63**, 1682 (1989).
[5] J. W. Dodd and T. C. Marshall, IEEE Trans. Plasma Sci. **PS-18**, 447 (1990); Li-Yi Lin and T. C. Marshall, Nucl. Instrum. Methods A **331**, 144 (1993).
[6] R. Bonifacio, B. W. J. McNeil, and P. Pierini, Phys. Rev. A **40**, 4467 (1989).
[7] W. M. Sharp, W. M. Fawley, S. S. Yu, A. M. Sessler, R. Bonifacio, and L. De Salvo Souza, Nucl. Instrum. Methods A **285**, 217 (1989).
[8] R. Bonifacio, N. Piovella, and B. W. J. McNeil, Phys. Rev. A **44**, 3441 (1991).
[9] G. T. Moore and N. Piovella, IEEE J. Quantum Electron. **QE-27**, 2522 (1991).
[10] S. J. Hahn and J. K. Lee, Nucl. Instrum. Methods A **331**, 390 (1993).
[11] R. M. Caloi, Phys. Rev. A **46**, 7934 (1992).
[12] R. Bonifacio and F. Casagrande, Nucl. Instrum. Methods A **239**, 36 (1985).
[13] R. Bonifacio, L. De Salvo Souza, P. Pierini, and N. Piovella, Nucl. Instrum. Methods A **296**, 358 (1990).
[14] S. Y. Cai, J. Cao, and A. Bhattacharjee, Phys. Rev. A **42**, 4120 (1990).
[15] N. M. Kroll and M. N. Rosenbluth, in *Physics of Quantum Electronics: Free-Electron Generators of Coherent Radiation*, edited by S. F. Jacobs, H. S. Pilloff, M. Sargent, M. O. Scully, and R. Sitzer (Addison-Wesley, Reading, MA, 1980), Vol. 7, p. 147; W. B. Colson, Nucl. Instrum. Methods A **250**, 168 (1986); M. N. Rosenbluth, H. V. Wong, and B. N. Moore, Phys. Fluids B **2**, 1635 (1990).
[16] C. Chen and R. C. Davidson, Phys. Rev. A **43**, 5541 (1991); L. Michel, A. Bourdier, and J. M. Buzzi, Nucl. Instrum. Methods A **304**, 465 (1991); G. Spindler and G. Renz, *ibid.* **304**, 492 (1991); S. Riyopoulos and C. M. Tang, Phys. Fluids **31**, 3387 (1988).
[17] Ya. L. Bogomolov, V. L. Bratman, N. S. Ginzburg, M. I. Petelin, and A. D. Yunakovsky, Opt. Commun. **36**, 209 (1981).
[18] W. B. Colson and R. A. Freedman, Opt. Commun. **46**, 37 (1983).
[19] N. S. Ginzburg and M. I. Petelin, Int. J. Electron. **59**, 291 (1985).
[20] T. M. Antonsen, in *Nonlinear Dynamics and Particle Acceleration (Tsukuba, Japan 1990),* edited by Y. H. Ichikawa and T. Tajima, AIP Conf. Proc. No. 230 (AIP, New York, 1991), p. 106; H. P. Freund and T. M. Antonsen, *Principles of Free-electron Lasers* (Chapman and Hall, London, 1992), p. 431.
[21] S. J. Hahn and J. K. Lee, Phys. Lett. A **176**, 339 (1993).
[22] H. G. Schuster, *Deterministic Chaos: An Introduction* (VCH Verlagsgesellschaft, Weinheim, 1989).
[23] J.-P. Eckmann, Rev. Mod. Phys. **53**, 643 (1981).
[24] The equation of the radiation field is given as follows: $\frac{d}{dz}\tilde{a} = i\eta a_w \left\langle \frac{e^{-i\theta}}{\gamma} \right\rangle - \alpha\tilde{a}$. See Eq. (2.3).
[25] K.-J. Kim, Phys. Rev. Lett. **57**, 1871 (1986); S. Krinsky and L. H. Yu, Phys. Rev. A **35**, 3406 (1987).
[26] H. Al-Abawi, F. A. Hopf, G. T. Moore, and M. O. Scully, Opt. Commun. **30**, 235 (1979).
[27] D. A. Jaroszynski, D. Oepts, A. F. G. van der Meer, P. M. van Amersfoort, and W. B. Colson, Nucl. Instrum. Methods A **296**, 480 (1990).
[28] D. A. Jaroszynski, R. J. Bakker, D. Oepts, A. F. G. van der Meer, and P. W. van Amersfoort, Nucl. Instrum. Methods A **331**, 52 (1993); Phys. Rev. Lett. **70**, 3412 (1993).
[29] S. Y. Cai and A. Bhattacharjee, Phys. Rev. A **43**, 6934 (1991); N. Piovella, Opt. Commun. **83**, 92 (1991).
[30] A. Ben-Mizarchi, I. Procaccia, N. Rosenburg, and A. Schmidt, Phys. Rev. A **31**, 1830 (1985).
[31] P. Y. Cheung, S. Donovan, and A. Y. Wong, Phys. Rev. Lett. **61**, 1360 (1988).
[32] R. Graham and S. Isermann, Phys. Rev. A **43**, 3982 (1991).
[33] T. H. Chung, H. S. Kim, and J. K. Lee, Nucl. Instrum. Methods A **331**, 482 (1993); T. H. Chung and J. K. Lee, J. Phys. Soc. Jpn. (to be published); H. S. Kim, S. J. Hahn, and J. K. Lee, *ibid.* **62**, 2334 (1993).